# ROTOR AIRFOIL AERODYNAMIC DESIGN METHOD AND TEST VERIFICATION

**He Long[1] , Sun Junfeng[2] , Zhang Weiguo[1] , Wu Jie[1]**

（1.China Aerodynamics Research & Development Center, Low Speed Aerodynamics Institute, Mianyang, Sichuan,621000, China；
2. China Aerodynamics Research & Development Center, Computational Aerodynamics Institute, Mianyang, Sichuan, 621000, China)

**Abstract**

Good airfoil design is a prerequisite for high performance rotor design. In order to establish the rotor airfoil design method and verify the wind tunnel data, this paper developed an efficient multi-objective and multi-constraint optimization design system for rotor airfoils, which is based on high-precision CFD analysis. And using OA309 as the baseline rotor airfoil, the CRA09 optimized rotor airfoil was designed successfully. Combined with the foundation of high-precision rotor airfoil stationary test technology, the CRA09 and OA309 rotor airfoils were tested in the S3MA high speed wind-tunnel of ONERA and the FL-21 high speed wind-tunnel of CARDC. Results indicate that, multi-objective and multi-constraint optimization design method developed in this study is reliable; CRA09 optimized airfoil provides better stationary performance than OA309 airfoil, in terms of maximum lift coefficient and lift over drag ratio.

Key words：rotor; optimization method; CRA09 airfoil; wind tunnel test

## 1. INTRODUCTION

The aerodynamic characteristics of the helicopter rotor are closely related to the design of the rotor airfoil. A refined airfoil can apparently improve the rotor hovering efficiency and also has a significant influence on forward flight speed, equivalent lift-drag ratio, maneuvering capability and acoustic radiation. Theory analyses and wind tunnel experiments [1][2] have contributed to various series of high-performance specific rotor airfoil and developed a corresponding airfoil library since 1960s, greatly meeting the aerodynamic performance objectives of the helicopter. Some typical series of rotor airfoil include the TsAGI series of TsAGI, the OA series of ONERA, the VR series of Boeing Vertol, the SC series of Sikorsky. Such series of airfoil have been widely applied on the rotor of the third and fourth generation helicopter, such as the OA3 airfoil of the NH90, the SC 1095 airfoil of the UH-60 Black Hawk and the S-76. At the beginning of the 21st century, the OA5 series of airfoil by ONERA and the TsAGI15 series by TsAGI have been developed. The aerodynamic characteristics of rotors are further improved by adopting the optimized airfoils, and show better performance over a wide range of Mach numbers.

In China, researches on rotor airfoil were started at the end of the last century [3]-[5]. A recently related development in the literature is the design of rotor airfoil and verification methods. However, technologies completing the methods of the design of rotor airfoil and verification are still lacking, limiting the capability of the designed rotor airfoils.

This paper is aiming at designing a kind of optimized rotor airfoil by multi-objective and multi-constrained optimization design, based on a series of classical technologies including the evolutionary algorithm, CST (Class-Shape Transformation) method and CFD (Computational Fluid Dynamics) method. Then, a correction method of high-speed wind tunnel is established and the verification method of wind tunnel test of airfoil is improved. Static characteristics of the optimized rotor airfoil have been verified in the high-speed wind tunnel in CARDC (China Aerodynamics Research and Development Center) and the ONERA-

S3MA wind tunnel.

## 2. METHODOLOGY

### 2.1 Airfoil Parameterization

Airfoil Parameterization is the foundation of airfoil design, aimed at setting design variables to acquire the data from the aerodynamic configuration of the airfoil. The parametric process is based on CST method [6]-[8]. This method can be easily used to control the number of design parameters and the critical parameters, including the leading edge radius, the camber distribution, the thickness distribution, the angle of trailing edge, the thickness of trailing edge, the section shape, the gradual transition and so on.

Considering $x$ and $y$ as the components of the airfoil configuration in the Cartesian coordinates, the complete configuration of the airfoil can be described in Eq. (1).

$$\varsigma = C_{N2}^{N1}(\psi)S(\psi) + \psi\Delta\xi \tag{1}$$

Where $C_{N2}^{N1}(\psi)$ and $S(\psi)$ are the class function and shape function, respectively. They are given in Eqs. (2) and (3).

$$C_{N2}^{N1}(\psi) = \psi^{N1}(1-\psi)^{N2} \tag{2}$$

$$S(\psi) = \sum_{i=1}^{n} A_i S_i(\psi) \tag{3}$$

Where

$$S_i(\psi) = K_i \psi^i (1-\psi)^{n-i} \tag{4}$$

$$K_i = \binom{n}{i} \tag{5}$$

And $\Psi$ and $\zeta$ represent the non-dimensional variables as Eqs. (6) and (7)

$$\psi = x/c \tag{6}$$

$$\varsigma = y/c \tag{7}$$

Moreover, $A_i$ is referred to the design parameter, where variable $i$ is the number of the points of the airfoil configuration within a considerable range, and $\xi$ is the non-dimensional variables given by Eq. (8)

$$\Delta\xi = \frac{y_{TE}}{c} \tag{8}$$

$y_{TE}$ is the thickness of the trailing edge and $c$ is the chord length of the airfoil. As for the round head airfoil, $N1$ equals to 0.5, and $N2$ equals to 2.0.

The fitting approximating method is used to simulate the correct outline of the rotor airfoil accurately, by giving twelve design variables of the upper and lower outline of the airfoil, respectively.

The variation of the leading and trailing edge can be defined by control functions as

$$S(0) = \sqrt{2R_{LE}/c} \tag{9}$$

$$S(1) = \tan(\beta) + \frac{y_{TE}}{c} \tag{10}$$

Where $S(0)$ and $S(1)$ are referred to the shape functions , $R_{LE}$ is the leading edge radius, $\beta$ are the angle of the trailing edge.

### 2.2 Numerical computation method and grid system

A self-developed program, MBNS2D (Multi-block Navier-Stokes two dimension) [9], based on RANS (Reynolds Average Navier-Stokes) equations, is used to analyze the aerodynamic characteristics of the airfoil. The RANS equations are discretized in space by cell-centered finite-volume method with the implementation of Roe's scheme, and the simulations are accelerated by multi-grid technology. A $\gamma$-$Re_\theta$ transition model [10] is provided in the computation process of the aerodynamic performance of the airfoil, in order to improve the precision of the calculation of the drag.

The generation and deformation of the grid system are automatically completed by the program using hyperbolic differential equation. The chord of the airfoil is set to 0.3m, and the distance of the first layer grid from the wall is set to $3\times10^{-5}$m. The wrap-around and normal-direction grids are composed by 767 elements and 127 elements, respectively, as shown in Figure 1.

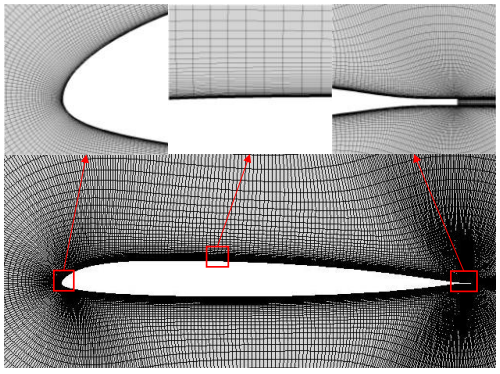

Figure 1. Sketch of computational grid for airfoil

### 2.3 Multi-objective optimization method based on evolutionary algorithm

The optimization method adopted in this paper is based on the evolutionary algorithm, the thought of multi-objective Pareto-optimal solutions [9][11] and the penalty function method. Initially, the design variables and the optimization space are encoded by the algorithm. After that, a random method is used to generate fixed-scale population and the individual fitness function of the population is calculated to identify the individual quality of the population. Furthermore, the process including selection, crossover and genetic manipulation for the population are performed and iterated to generate the final Pareto solutions.

The practical problems are constrained using the penalty function method to reduce the selection probability of their descendants and limit the population in the region of the feasible solution by punishing the individual fitness value against the constraint. However, if the constraint condition is strict excessively, the feasible solution may hardly be searched by using this way. Therefore, for the infeasible solution of the intermediate population, another way is to perform uncontrolled sequencing to retain the good individuals of the infeasible solution and promote the population to the region of the feasible solution as soon as possible. The generated feasible solution will be retained as an elite individual, further evolving the population into Pareto solutions.

### 2.4 Optimization results

The optimized airfoil in the study takes OA309 as the baseline. The maximum thickness is 8.8%$c$ at 32%$c$ of the airfoil and the maximum camber is 1.3%$c$ at 17%$c$ of the airfoil. This study tries to improve the forward flight and maneuvering capability without decreasing the thickness of the airfoil and the hover performance of the rotor. Details of the optimization method are shown in Table 1.

Table1 Design states, objective functions and constraint conditions

| Serial number | Improve performance | Design states | Objective functions | constraint conditions |
|---|---|---|---|---|
| 1 | Forward flight performance | $M_{DD0}$ | $M_{DD0}\geq M_{DD0b}$ | $C_m\leq 0.02$ |
| 2 | Maneuverability | $M$=0.3, 0.4, 0.5, 0.6 | $C_{Lmax}\geq C_{Lmaxb}$, $(C_L/C_D)_{max}\geq (C_L/C_D)_{maxb}$ | $C_D\leq C_{D\,b}$, $C_m\leq 0.02$ |
| 3 | Hover performance | $C_L$=0.6, $M$=0.5; $C_L$=0.6, $M$=0.6 | $(C_L/C_D)_{max}\geq (C_L/C_D)_{maxb}$ | $C_L\geq C_{L\,b}$, $C_m\leq 0.02$ |
| 4 | Thickness | -- | -- | $t_{max}\geq t_{maxb}$ |

Where the subscript b indicates the performance index of the baseline airfoil OA309, and the symbols $M_{DD0}$, $C_m$, $C_{Lmax}$, $(C_L/C_D)_{max}$, $t_{max}$ represent the zero-lift drag divergent Mach number, the zero-lift pitching moment, the maximum lift coefficient, the maximum lift-drag ratio, the maximum thickness, respectively.

In order to satisfy the multi-objective design and sufficient constraint condition, the value of the optimized parameters, including population size, crossover probability, mutation rate and the maximum generation, are defined as 120, 0.8, 0.2, 400, respectively.

The Pareto solutions of optimized result are given in Figure 2. For ease of understanding, the red balls and the purple cube represent the sampling points and initial airfoil, respectively. The blue ball refers to the

Pareto solutions of optimized result. Considering the comprehensive characteristics of hover, forward flight and maneuverability, the design select the green balls mean better maneuverability from the Pareto solutions as the final optimized result. The corresponding optimized airfoil, shown in Figure 3, is named as CRA09. The maximum thickness is 9%$c$ at 32%$c$ of the airfoil and the maximum camber is 1.4%$c$ at 17%$c$ of the airfoil, where $c$ is the chord length.

Table 2 illustrates the comparison between the performances of the two sets of airfoils. As described in Table 2, the maximum lift coefficient $C_{Lmax}$ and the maximum lift-drag ratio $(C_L/C_D)_{max}$ of CRA09 are significantly improved. For the case M=0.6, $C_{Lmax}$ and $(C_L/C_D)_{max}$ are improved by 4.1% and 11.1%, respectively. While the zero-lift drag divergent Mach number $M_{DD0}$ ($C_L$=0) is decreased by 1.2%.

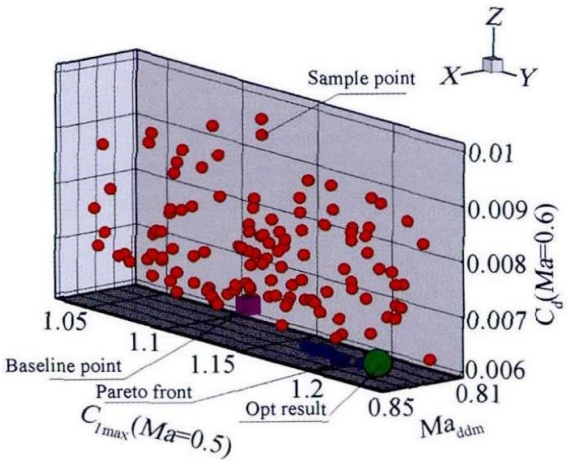


Figure 2. Pareto solutions of optimized result

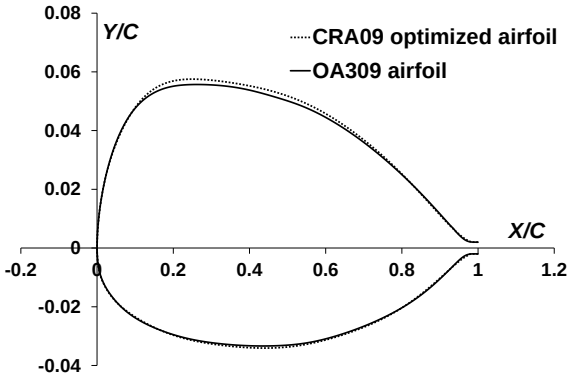


Figure 3. Comparison between OA309 and CRA09 in configuration

Table 2. Comparison between performance of OA309 and CRA09

| Aerodynamic parameter | OA309 | CRA09 | Improvement |
|---|---|---|---|
| $C_{Lmax}(M=0.3)$ | 1.476 | 1.50 | 1.6% |
| $C_{Lmax}(M=0.4)$ | 1.307 | 1.307 | 0.0% |
| $C_{Lmax}(M=0.5)$ | 1.144 | 1.170 | 2.3% |
| $C_{Lmax}(M=0.6)$ | 0.939 | 0.978 | 4.1% |
| $(C_L/C_D)_{max}(M=0.3)$ | 97.7 | 98.8 | 1.1% |
| $(C_L/C_D)_{max}(M=0.4)$ | 102.8 | 104.5 | 1.7% |
| $(C_L/C_D)_{max}(M=0.5)$ | 105.1 | 108.4 | 3.1% |
| $(C_L/C_D)_{max}(M=0.6)$ | 87.5 | 97.2 | 11.1% |
| $M_{DD0}$ | 0.84 | 0.83 | -1.2% |
| $C_{m0}(M_{DD0})$ | -0.016 | -0.013 | 17.5% |
| $(C_L/C_D)_{max}$ ($C_L$=0.6, $M$=0.5) | 89.9 | 93.0 | 3.4% |
| $(C_L/C_D)_{max}$ ($C_L$=0.6, $M$=0.6) | 87.27 | 94.0 | 6.5% |
| $t/c$ | 0.088 | 0.09 | -- |

## 3. VERIFICATION IN CARDC FL-21 HIGH-SPEED WIND TUNNEL

### 3.1 Test equipment

CARDC FL-21 wind tunnel [12] is a transonic wind tunnel with the length of 1.775m in the test section. Both the width and the height of the test section are 0.6m. The test about the baseline airfoil OA309 conducted in this wind tunnel is shown as Figure 4.

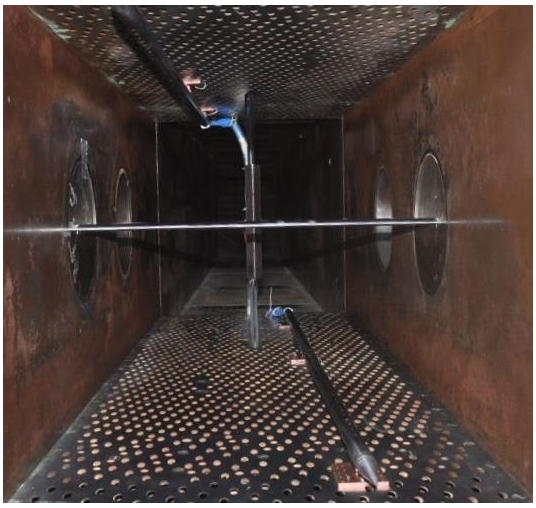

Figure 4. OA309 test filed in FL-21 wind tunnel

The span and the chord of the test article of OA309 are 600mm and 150mm respectively. The maximum thickness of the airfoil is 13.5mm. Besides that, there are fifty-three and fifty-one pressure taps distributed on the upper and lower surface of the airfoil, respectively. Figure 5 presents the distribution of these pressure taps on the model. The test article is mounted on the side pivoted windows crossing the wind tunnel as given by Figure 4.

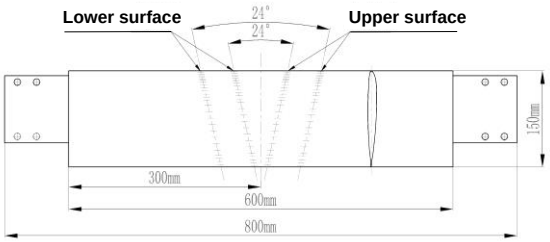


Figure 5. Distribution of pressure taps on the model in CARDC

Figure 6 illustrates the measurement device used to test the pressure of the airfoil wake, named by wake rake. There are forty-eight total pressure probes and five needles with static pressure taps distributed around. The distance from the top of the needles to the trailing edge of the airfoil are 262mm, 1.75 times of the chord length of the model.

Figure 6. Wake rake

Two sets of wall pressure test equipment are installed on ventilation area of the ceiling and the ground in the test section. There are forty wall pressure taps placed in the inflow direction on each set of equipment, away from the highly unsteady flow area near the vent holes. The distance is 53mm from the pressure taps to the wall. The longitudinal pressure gradient at the most upstream wall pressure tap approaches to zero to avoid affecting the accuracy of the angle of attack correction. The most downstream wall pressure tap is located about twice the chord length at the trailing edge of the model, ensuring the accuracy of the speed correction. The body blockage of the airfoil is 2.25% at an angle of attack of 0°. Figure 7 shows the layout of the test model, wake rake and the wall pressure test equipment in the wind tunnel.

A set of PSI9016 EPSV (Electronic Pressure Scanner Valve) is introduced to acquire the static pressure of the airfoil surface and the wall, along with the total and static pressure of the airfoil wake. This system has been verified to be well stable and with digital temperature compensation function. The precision is ±0.05% for full scale.

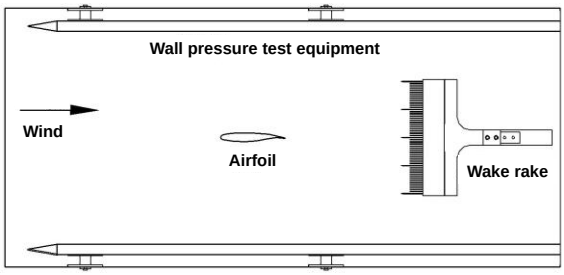


Figure 7. Layout of test model and equipment

### 3.2 Wind tunnel wall interference correction method

The wind tunnel wall always results in the deviation of the acquired dynamic data. In order to correct the deviation, this paper discusses the lift effect correction method.

The airfoil is interfered seriously by the wind tunnel wall due to the limited size of the high-speed wind tunnel and the high Mach number, along with the vent holes and grooves on the ceiling and ground, leading to the test data lack of accuracy. Therefore the wind tunnel wall interference method is introduced to correct the test data of the aerodynamic force. The single parameter linear wall pressure method[12]-[15] is used to perform the correction. The far-field interference velocity potential $\Phi_m$ of the model near the wall is defined by Eq. (11). Similar method is also used in ONERA, but slightly differs in solution procedure, where CARDC uses numerical method

and ONERA uses analysis method.

$$\phi_m = -\frac{1}{2\pi}\sum_K G_K \operatorname{arctg}\left[\frac{\beta(y-y_K)}{x-x_K}\right] + \frac{1}{2\pi\beta}\sum_K V_K \frac{x-x_K}{R_K^2} + \frac{1}{2\pi\beta}\sum_K Q_K \log R_K \tag{11}$$

Where $G_k$, $Q_K$ and $V_K$ are the vortex strength, source strength and dipole strength, respectively, as shown in Eqs. (13), (14) and (15)

$$R_K = \sqrt{(x-x_K)^2 + \beta^2(y-y_K)^2} \tag{12}$$

$$\sum_K G_K = 0.5 b_a C_{Lu} \tag{13}$$

$$\sum_K Q_K = 0.5 b_a C_{Du} \tag{14}$$

$$\sum_K V_K = V \tag{15}$$

$C_{Lu}$ and $C_{Du}$ represent the tested lift coefficient and drag coefficient. The subscript $K$ is the number of the singular points. Besides, $b_a$ and $V$ are the chord length and the section area of the model.

## 4. VERIFICATION IN ONERA S3MA HIGH-SPEED WIND TUNNEL

The comparison test of the OA309 airfoil and CRA09 optimized airfoil is performed in the VCP nozzle of the S3 wind tunnel in Modane-Avrieux (S3MA). Especially, the VCP test section is designed for testing the performance of two-dimension airfoil, and the height and the width of the test section are 0.78m and 0.56m, respectively. Figure 8 presents the layout of the test section. The vertical walls are solid and the horizontal walls have geometric porosity of 9.7%.

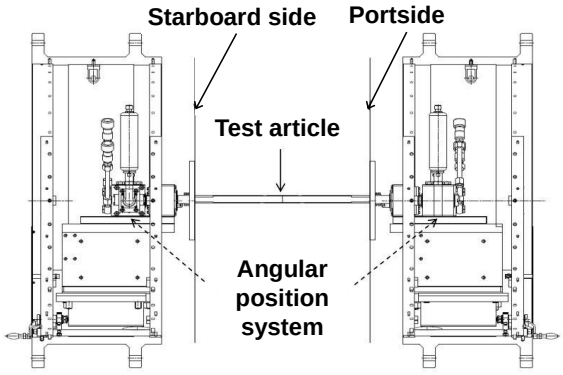


Figure 8. Test section for two-dimension airfoil in ONERA S3MA wind tunnel

Figure 9 exhibits two sets of the test models of OA309 and CAR09.The span and the chord are 560mm and 210mm, respectively. The maximum thickness of the airfoil is 18.9mm. Moreover, there are sixty and forty pressure taps distributed on the upper and lower surface of the airfoil, respectively. Figure 10 presents the distribution of these pressure taps on the model. The density of pressure taps increases along the leading edge of the airfoil. The pressure taps of the upper and lower surface are distributed as slashes symmetrically about the central axes. The angle of the slash and the axes is 10°. Meanwhile, the test model is also mounted on the side pivoted windows crossing the wind tunnel. The trailing edge of the airfoil is 355mm away from the top of the wake test device, 1.55 times of the model chord.

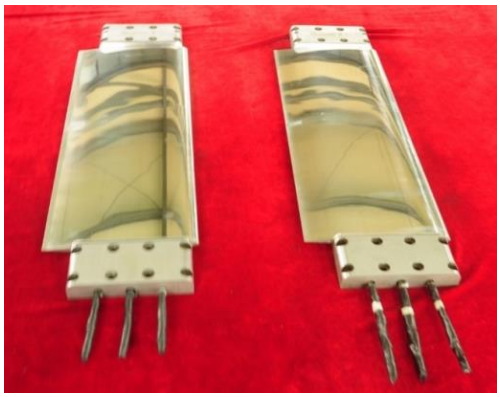

Figure 9. Two sets of airfoil models of OA309 and CAR09

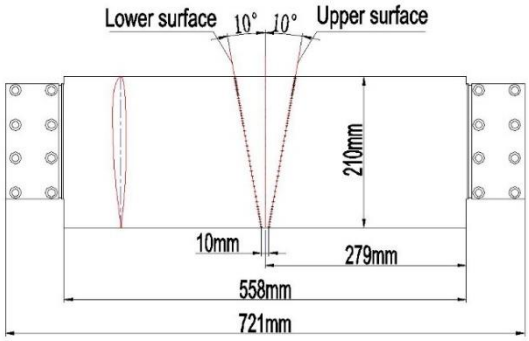


Figure 10. Distribution of pressure taps on the model in ONERA

Similarly, the total pressure of the airfoil wake and the static pressure of the airfoil wake and the wind tunnel wall are measured by wake test device and wall

pressure test equipment as mentioned in Section 3.1. The pressure of the airfoil surface and the wall pressure are measured by PSI pressure measurement system. In addition, the static pressure of the wake and the total pressure in the tunnel are tested using Kulite pressure sensors. Both the PSI pressure measurement system and the Kulite pressure sensor are differential pressure sensors. Therefore, the reference pressure is introduced to the procedure in the test.

## 5. RESULTS AND DISCUSSION

### 5.1. Comparison of different wind tunnel wall interference correction methods

The method to correct wind tunnel wall interference of the test data of the baseline airfoil OA309 in CARDC FL-21 wind tunnel is mentioned in section 3.2. The correction results are given in Figure 11, Figure 12 and Figure 13. It can be clearly seen from Figure 11 that in the case of typical Mach numbers (Ma = 0.4 and 0.6), the slope of the lift curve in FL-21 wind tunnel with the wall pressure correction is consistent with the S3MA wind tunnel data, and the difference between the two is only about 2%. Therefore, for high-speed wind tunnels, the wall interference can be corrected by wall pressure correction method. And the correction of the angle of attack based on the quarter chord is very considerable, because the slope of the lift curve with wall pressure correction is increased by 10% and the angle of attack corresponding to the maximum lift coefficient is very close. However, the correction for Mach number ($\triangle M$ is less than 0.1%)), lift, drag and pitching moment coefficients is very small. Figure 12 presents that the corrected drag divergence angle of attack is in good agreement with the ONERA data. When the angle of attack is from -4° to 11°, the drag coefficient is well matched. Figure 13 illustrates that lift over drag ratio curve has been greatly improved compared with that before the correction. Therefore, the method can effectively correct the rotor airfoil test data, especially the angle of attack of the model.

It can be seen from Figure 11 and Figure 13 that the corrected maximum lift coefficient and maximum lift over drag ratio are smaller than the data of the French S3MA wind tunnel. This paper considers that this is related to the test Reynolds number. Because the Reynolds number of S3MA wind tunnel is higher than the FL-21 wind tunnel, and as the wind speed increases, the test Reynolds number of the S3MA wind tunnel increases accordingly. Therefore, due to the low test Reynolds number of the FL-21 wind tunnel, the corrected maximum lift coefficient is smaller and the drag coefficient is larger than the S3MA wind tunnel data, resulting in a maximum lift over drag ratio which is significantly smaller than S3MA wind tunnel data. This problem can be solved by increasing the test Reynolds number or the Reynolds number correction method.

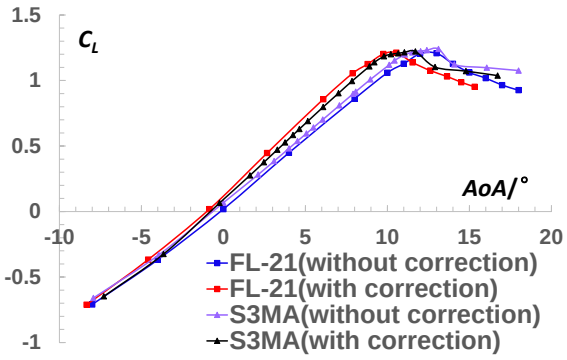


(a) M=0.4

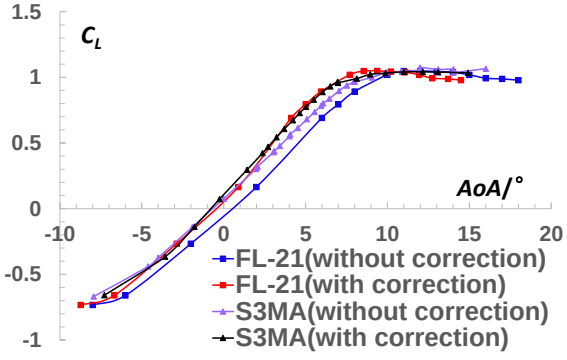


(b) M=0.6

Figure 11. Comparison of $C_L$ of OA309 airfoil in FL-21 wind tunnel and S3MA wind tunnel

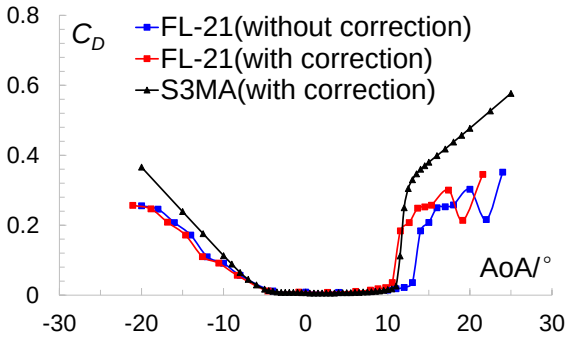


Figure 12. Comparison of $C_D$ of OA309 airfoil in FL-21 wind tunnel and S3MA wind tunnel (M=0.4)

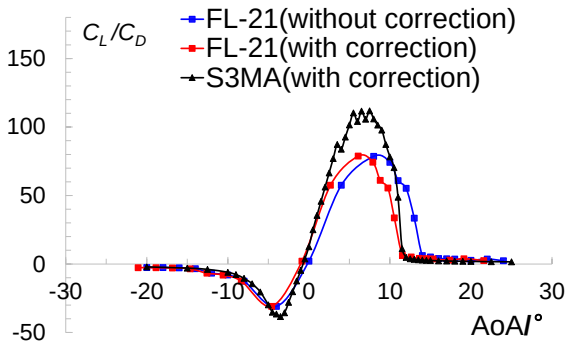


Figure 13. Comparison of $C_L$ /$C_D$ of OA309 airfoil in FL-21 wind tunnel and S3MA wind tunnel (M=0.4)

### 5.2. Comparison of aerodynamic performance between CRA09 optimized airfoil and OA309 airfoil

Aerodynamic coefficients of the two airfoils obtained for $M$= 0. 6 are compared in Figure 14, Figure 15, Figure 16 and Figure 17. It can be seen from Figure 14 that the lift coefficient of the CRA09 optimized airfoil is slightly larger than the lift coefficient of the OA309 airfoil. And at the post stall position (AOA=9°), the CRA09 optimized airfoil lift coefficient is 1.07, which is superior to 1.03 of the OA309 airfoil. This is mainly due to the expansion of the pressure peak on the upper surface of the CRA09 optimized airfoil. Figure 15 shows that the drag coefficient of the CRA09 optimized airfoil is smaller than that of the OA309 airfoil at an angle of attack of 0°~13°. And in the post stall position (AOA=9°), the drag coefficient of the CRA09 optimized airfoil is 0.078, and the drag coefficient of the OA309 airfoil is 0.101.

Figure 16 exhibits that the lift over drag ratio is also higher with CRA09 optimized airfoil over a wide range of AoA. Its maximum lift over drag ratio reaches 95 against 80 for OA309 airfoil. Figure 17 presents that the pitching moment characteristic of the CRA09 optimized airfoil is worse than that of the OA309 airfoil at an angle of attack of -5°~4.4°, but it is better than the OA309 airfoil between 4.4° and 10°.

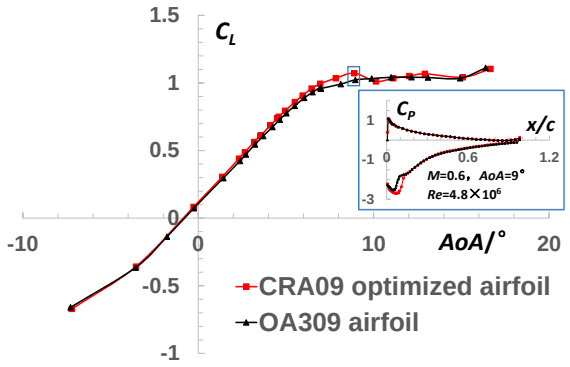


Figure 14. Comparison of $C_L$ between CRA09 optimized airfoil and OA309 airfoil (M=0.6)

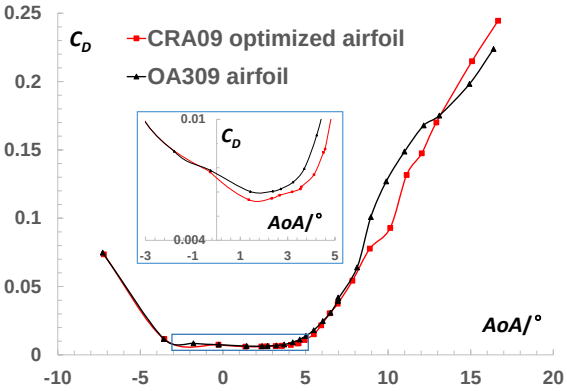


Figure 15. Comparison of $C_D$ between CRA09 optimized airfoil and OA309 airfoil (M=0.6)

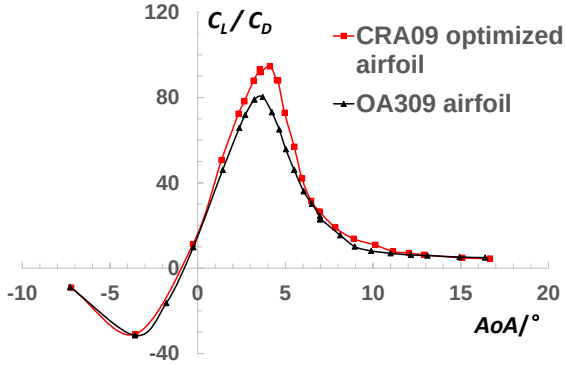


Figure 16. Comparison of $C_L$/$C_D$ between CRA09 optimized airfoil and OA309 airfoil (M=0.6)

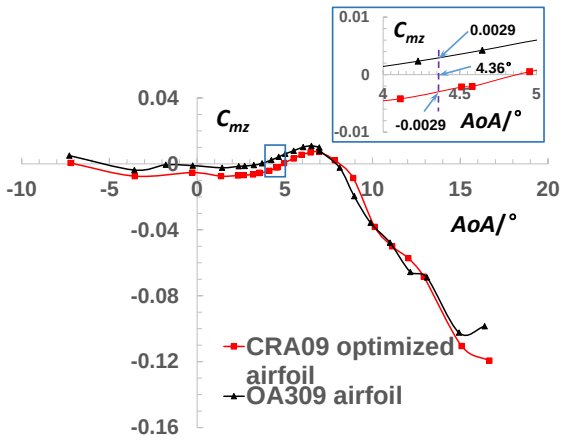


Figure 17. Comparison of $C_m$ between CRA09 optimized airfoil and OA309 airfoil (M=0.6)

To provide a more overall review of the two airfoils, the results are compared in terms of maximum lift and maximum lift over drag ratio as a function of the Mach number in Figure18 and Figure19, respectively. It can be seen from Figure 18 that as the Mach number increases, the maximum lift coefficient of both airfoils shows a decreasing trend. And at $M$=0.4 and 0.6, the maximum lift coefficient of the CRA09 optimized airfoil is slightly higher than that of the OA309 airfoil. Figure 19 illustrates that at M = 0.4, 0.6 and 0.8, the maximum lift over drag ratio of the CRA09 optimized airfoil is greater than that of the OA309 airfoil, and it reaches the maximum when M=0.6.

Figure 20 represents the drag coefficient at $C_L$= 0 as a function of the Mach numbers. The two airfoils provide very similar $C_{D0}$ for $M$≤0. 6. Then, for $M$≥0. 7, CRA09 optimized airfoil gives slightly higher drag coefficients but the trends of the two curves are similar. In particular, the drag divergence Mach number of CRA09 optimized airfoil is probably similar to the one of OA309 airfoil (i.e. $M_{DD0}$=0.84), although the discretization in Mach numbers of CRA09 optimized airfoil is not fine enough to calculate accurately its $M_{DD0}$.

Figure 21 compares the zero-lift pitching moment of the two airfoils as a function of the Mach number. The effect of the higher camber of CRA09 optimized airfoil is clearly visible. While OA309 airfoil has been designed to keep the pitching moment as low as possible ($C_{m0}$≈0.001), CRA09 optimized airfoil produces a higher pitching moment. This provides higher performance in terms of maximum lift and lift over drag ratio at moderate Mach number, but could be damageable in unsteady helicopter rotor flow conditions because of too high torsion deformation. This also illustrates that there is a contradiction between the optimization goals of the rotor airfoil. If the maximum lift coefficient is increased, the zero-lift drag divergence Mach number will decrease, and the zero-lift torque coefficient will increase.

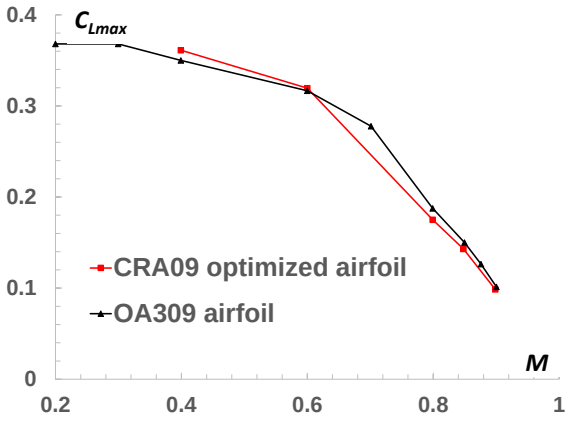


Figure 18. Comparison of $C_{Lmax}$ between CRA09 optimized airfoil and OA309 airfoil

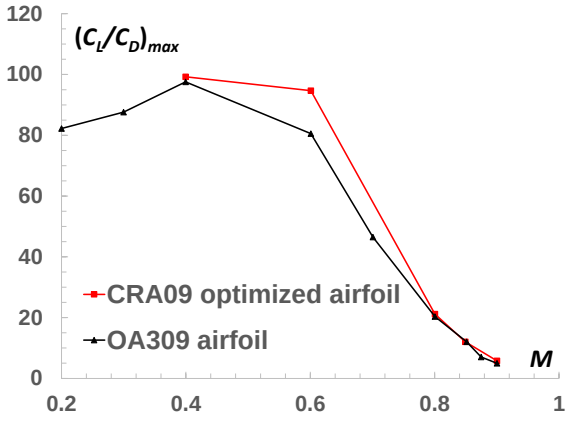


Figure 19. Comparison of $(C_L/C_D)_{max}$ between CRA09 optimized airfoil and OA309 airfoil

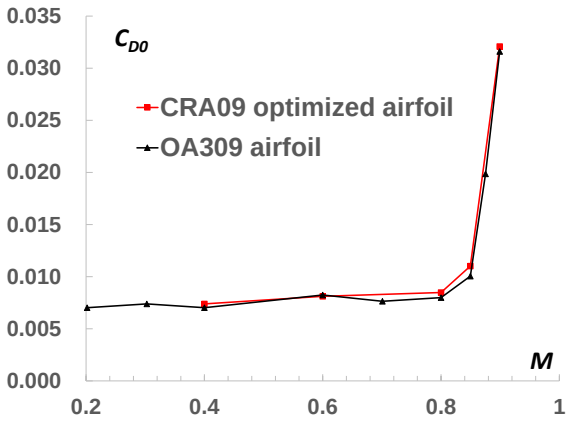


Figure 20. Comparison of $C_{D0}$ between CRA09 optimized airfoil and OA309 airfoil

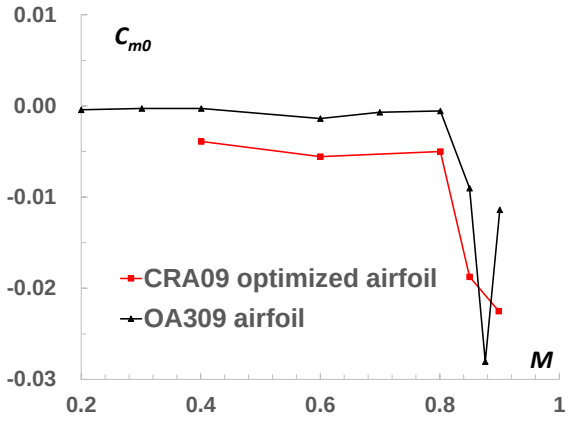


Figure 21. Comparison of $C_{m0}$ between CRA09 optimized airfoil and OA309 airfoil

## 6. CONCLUSION

1） The wind tunnel test results of CRA09 optimized airfoil and OA309 airfoil are basically consistent with the numerical calculation results in the optimization process.

2） The multi-objective and multi-constraint optimization design method developed in this study is reliable.

3） The single parameter linear wall pressure method can quickly correct the wall interference of the rotor airfoil successfully. It is an effective means to solve the wall interference of the rotor airfoil high-speed test .

4） CRA09 optimized airfoil provides better static performance than OA309 airfoil, in terms of maximum lift coefficient and lift over drag ratio. And dynamic test should be conducted later to verify the dynamic aerodynamic characteristics of the CRA09 optimized airfoil.

## References

[1] Li W, Krist S, Camberll R. Transonic airfoil shape optimization in preliminary design environment[R]. AIAA-2004-4629, 2004.

[2] Padula S L, Li W. Options for robust airfoil optimization under uncertainty[R]. AIAA-2002-5602, 2002.

[3] Shang Keming. Research on Aerodynamic Design Method for Helicopter Rotor Airfoils[D]. Nanjing：Nanjing University of Aeronautics and Astronautics，2009.

[4] Yuan Honggang，Yang Yongdong，Yang Jiong. et al. Experimental investigation on aerodynamic performance of one typical helicopter rotor airfoil[J]. Journal of Experiments in Fluid Mechanics.2013,27(1):20-24.

[5] Wang Qing，Zhao Qijun. Synthetical optimization design of rotor airfoil by genetic algotithm[J]. Journal of Aerospace Power. 2016, 31(6):1486-1495.

[6] Bogue D, Crist N. CST transonic optimization using tranair++[R]. AIAA-2008-321, 2008.

[7] Ceze M, Hayashi M,Volpe E. A study of the CST parameterization characteristics[R]. AIAA-2009-3767, 2009.

[8] Kulfan B M. A universal parametric geometry representation method: CST[R]. AIAA-2007-0062, 2007.

[9] Sun Junfeng，Liu Gang，Jiang Xiong. et al. Research of rotor airfoil design optimization based on the Kriging model[J]. ACTA AERODYNAMICA SINICA. 2013，31(4)：437-441.

[10] Menter F R, Kuntz M, Langtry R. Ten Years of Industrial Experience with the SST Turbulence Model[J]. Turbulence, Heat and Mass Transfer, 2003(4):625–632.

[11] Holst T L. Genetic algorithms applied to multi-objective aerospace shape optimization[R].

AIAA-2004-6512, 2004.

[12] He Long, Wu Jie, Zhang Weiguo, et al. Correction research of the wall pressure method for rotor airfoil in high speed wind tunnel[J]. Journal of Nanjing University of Aeronautics & Astronautics，2017，49(2)：183-188.

[13] Mokry M，Ohman L.H. Application of the Fast fourier transform to two dimensional wind tunnel wall interference[J]. Aircraft，1980,17(6)：402-408.

[14] Mokry M，Digney J.R. Poolet R.J.D. Doublet panel method for half model wind tunnel corrections[J]. AIRCRAFT，1987，24(5)：322-327.

[15] Fan Zhaolin，Cui Naiming，Yun Qilin. Application of the wall pressure method to wall interference correctons for model tests at high angle of attack in high speed wind tunnel[J]. Acta Aerodynamica Sinica, 1991,9(2):243-250.